NJC

PAPER

View Article Online
View Journal | View Issue

Cite this: *New J. Chem.*, 2022, **46**, 13296

Fe–Ni–Co trimetallic oxide hierarchical nanospheres as high-performance bifunctional electrocatalysts for water electrolysis†

Wenqing Zheng,‡[a] Xinzhi Ma,‡[b] Han Sun,[a] Xinping Li,[a] Yu Zhang,[a] Zhuoxun Yin, *[a] Wei Chen*[a] and Yang Zhou[c]

Received 11th April 2022,
Accepted 8th June 2022

DOI: 10.1039/d2nj01762h

rsc.li/njc

Water electrolysis is one of the most promising approaches for producing hydrogen. However, the OER, kinetics are sluggish and necessitate highly efficient electrocatalysts to speed up the reaction. In this work, we used NiCo glycerate solid nanospheres as a precursor to construct Fe–Ni–Co trimetallic oxide nanospheres utilizing a solvothermal-annealing and stirring technique. The oxygen evolution reaction (OER) activity of the Fe–Ni–Co spheres was greatly enhanced after Fe doping. Among these samples, the FeNiCo-15 hierarchical yolk–shell spheres needed overpotentials of only 204 and 178 mV for the OER and HER, respectively, to drive a current density of 10 mA cm^{-2}, and showed good electrochemical stability. Further, it also presented superior electrocatalytic activity in terms of full water splitting, which was comparable to the integrated performance of the Pt|IrO$_2$ couple. A cell voltage of only 1.61 V was required to attain a current density of 10 mA cm^{-2}. This paper provides a promising method for developing efficient bifunctional electrocatalysts driving redox electrocatalysis.

1 Introduction

Energy and the environment are one of the most important issues of this era, and global demand for energy has been growing rapidly. However, so far most of the energy comes from limited reserves of fossil fuels, which is unsustainable.[1] With reduction of fossil fuel resources and the increases of energy demand, new methods for various types of energy production and utilization are valued, and hydrogen is considered as the ideal clean energy for the future.[2] Water electrolysis has received much attention as a representative energy conversion technique.[3] Electrolysis hydrolysis involves two semi-reactions under alkaline conditions: hydrogen evolution reaction (HER, $4H_2O + 4e^- \rightarrow 2H_2 + 4OH^-$) and oxygen evolution reaction (OER, $4OH^- \rightarrow O_2 + 2H_2O + 4e^-$), which make the energy conversion efficiency very limited due to the high energy barrier. In addition, the cost to prepare catalysts that met each semi-reaction single performance requirement was high, and researchers began to look for electrocatalysts capable of having dual functions of both the HER and OER in the same electrolyte, which would make water decomposition cost-effective for good practical application.[4]

However, Pt-based catalysts generally exhibit significant HER activity, but exhibit poor OER activity, while Ir-based catalysts show only good OER activity. Moreover, due to their high cost and scarcity, it is unrealistic to use them on an industrial scale.[5] In order to find electrocatalysts with abundant resources, low cost, high activity and stability, many research studies have been conducted to replace precious metal materials.[6] In addition, the use of different types of electrocatalysts in an integrated electrolytic cell may cause a mismatch between catalytic activity and stability.[7] Therefore, it is necessary to explore a new type of bifunctional electrocatalyst based on materials that are low cost and highly abundant in the earth, which should have a lower overpotential and a better water decomposition durability.

Recently, the development of the first row of transition metal (Fe, Co, Ni, *etc.*) materials abundant in the crust to replace precious metal materials as OER catalysts has attracted great interest. These materials include transition metal oxides,[8,9] transition metal hydroxides[10] and other transition metal compounds.[11] In particular, iron doped transition metal oxides have been reported as high efficiency electrocatalysts that exhibit excellent catalytic properties due to their beneficial adsorption of hydrogen ions and binding into H_2 molecules. In

---

[a] *College of Chemistry and Chemical Engineering, Qiqihar University, Qiqihar 161006, China. E-mail: yzx@qqhru.edu.cn*

[b] *Ministry of Education and School of Physics and Electronic Engineering, Harbin Normal University, Harbin 150025, China. E-mail: maxz@hrbnu.edu.cn*

[c] *College of Science, Qiqihar University, Qiqihar 161006, China. E-mail: 373133430@qq.com*

† Electronic supplementary information (ESI) available. See DOI: **https://doi.org/10.1039/d2nj01762h**

‡ These authors made equal contributions to this work.

addition, positively charged Fe atoms in the catalyst are capable of capturing electrons,[12] and these properties endow transition metal oxides with catalytic properties suitable for overall water electrolysis. Wang *et al.*[13] employed a one-step hydrothermal method using nickel chloride and cobalt chloride and synthesized binary metal oxides (Fe-VOx) with a highly crystalline phase. This led to the formation of a homogeneous spherical surface morphology, where Fe-VOx exhibited excellent electrochemical properties requiring only 160 and 300 mV overpotentials at current densities of 10 and 300 mA cm^{-2}, respectively. Friebel *et al.*[14] discovered that the OER activity of $Ni_{1-x}Fe_xOOH$ is 500-fold stronger than that of its pure Ni and Fe parent compounds when it is utilized as an OER catalyst. In addition, they noticed that the real OER active sites were transformed from Ni^{3+} to Fe^{3+} in $Ni_{1-x}Fe_xOOH$. Michaela S. Burke[15] found that the turnover frequency of $Co_{1-x}Fe_xOOH$ when $x \approx 0.6–0.7$ is about 100 times higher than that of $Co_{1-x}Fe_xOOH$ when $x = 0$. The excellent performance can be attributed to the following: the inherent properties of transition metal oxides, the presence of bimetallic synergistic effects, the special morphology design and a more electroactive surface/redox center after iron doping, which show better electrocatalytic performance.[16–21]

Herein, we designed and prepared a kind of Fe–Ni–Co nanospheres with a yolk–shell structure: after a period of ion exchange processing, iron ions enter and change the appearance of solid glycerol isopropanol spheres formed by nickel and cobalt ions *via* solvothermal treatment. The Fe–Ni–Co nanospheres have a larger specific surface area and more active sites due to their unique sheet-like cross morphology and more holes formed after iron doping.[22] The positively charged Fe atoms in the catalyst capture electrons and the cathode electrochemical treatment makes the catalyst surface form a transition metal hydroxide shell as a catalytically active shell for oxygen evolution,[23] which jointly promote the electrolysis of water and can be used as a dual-functional catalyst that can exhibit excellent catalytic performance in alkaline solutions.

2 Experimental section

Materials

The reagents we used were all of analytical grade and utilized directly with no further purification. $Co(NO_3)_2·6H_2O$, $Ni(NO_3)_2·6H_2O$, glycerol, isopropanol, TAA, and potassium hydroxide were obtained from Guangfu Fine Chemical Research Institute (Tianjin, China). We obtained the commercial IrO_2 catalyst from Macklin Biochemical Co., Ltd. Carbon paper was obtained from Hesen Electric Co., Ltd (Shanghai, China). The commercial graphite rod and Ag/AgCl (KCl saturated) electrode were acquired from AIDA Science-Technology Development Co., Ltd (Tianjin, China). We used ultrapure water (>18 MΩ) to prepare all the aqueous solutions.

Synthesis of NiCo solid glycerol isopropanol spheres

A total of 2 mmol of $Co(NO_3)_2·6H_2O$ and $Ni(NO_3)_2·6H_2O$ with different molar ratios were dissolved in a mixed solution of 7 mL glycerol and 25 mL isopropanol to get a transparent pink solution, which was then transferred to a stainless steel autoclave lined with Teflon and kept at a temperature of 180 °C for 6 h. Then the autoclave was cooled down naturally to room temperature, and the precipitate was washed with ethanol several times and dried in an oven at a temperature of 60 °C.

Synthesis of Fe–Ni–Co hierarchical yolk–shell spheres

40 mg of NiCo precursor and 120 mg of ferrous sulfate were mixed, dissolved in 30 mL of deionized water, ultrasonicated for 30 min, and kept soaking at room temperature for 15 h (denoted as FeNiCo-15). Then the mixture was washed with ethanol and water many times after the reaction was completed, and dried in a vacuum drying oven overnight to obtain a reddish brown powder. The above product was annealed in air at 500 °C for 2 h, and then hierarchical nanosheet-based FeNiCo-15 yolk–shell spheres were obtained. For the convenience of comparison, we also prepared samples soaked for 5, 10 and 20 hours, respectively. For convenience, hereafter they are denoted as FeNiCo-5, FeNiCo-10, and FeNiCo-20. The atomic ratios of FeNiCo-X are listed in Table S1 (ESI†).

Electrochemical measurements

Electrochemical measurements were conducted in a three-electrode system at an electrochemical station (CHI660E, CH Instruments, USA). The three electrodes include carbon paper which was used as the working electrode (1 cm^2), a graphite rod as the counter electrode and a Ag/AgCl (KCl saturated) electrode as the reference electrode. The loading mass of the catalysts was around 3.5 mg cm^{-2} for all the working electrodes. Electrochemical measurements of the catalysts were conducted in 1 M KOH solution using the method of purging the electrolyte with N_2 gas for 30 min. Linear sweep voltammetry (LSV) at a scanning rate of 2 mV s^{-1} was utilized to obtain the polarization curves. Chronopotentiometric measurements were conducted to test the long-term stability. The equation adopted to calibrate all the measured potentials to the RHE is as follows:

$$E(\text{RHE}) = E(\text{Hg/HgO}) + 0.098\ \text{V} + 0.059 \times \text{pH}. \qquad (1)$$

Structural characterization

Scanning electron microscopy (SEM) images were recorded with the use of a HITACHI SU8000 operating at 15 keV. Transmission electron microscopy (TEM) images were recorded on an FEI Tecnai-F20 transmission electron microscope fitted with a Gatan imaging filter (GIF). A Thermo ESCALAB 250 X-ray photoelectron spectrometer (XPS) was utilized to perform elemental analysis of the samples. X-ray diffraction (XRD) was carried out on an X'Pert Pro diffractometer with Cu Kα radiation (λ = 1.5418 Å). By means of energy dispersive X-ray spectrometry (EDS) and inductively coupled plasma optical emission spectrometry (ICP-OES), the metal content in the Fe–Ni–Co catalysts can be detected. High-resolution TEM (HR-TEM) and element mapping were performed using an FEI Tecnai G2 F20 S-Twin (acceleration voltage of 200 kV) electron microscope equipped with an energy-dispersive X-ray spectroscopy detector.

3 Results and discussion

In order to obtain the structural information of the composites after Fe doping, the samples were analyzed by XRD, and the experimental results are shown in Fig. 1. As can be seen from the XRD patterns, all diffraction peaks were indexed as $NiCo_2O_4$, proving that the product is mainly composed of the cubic phase $NiCo_2O_4$. Since it belongs to the spinel structure, the characteristic diffraction peaks with a spinel structure appear around 2θ = 18.18°, 30.02°, 36.14°, 43.82°, 55.18°, 58.74° and 65.06° in the XRD spectra of the samples, which are assigned to (111), (220), (311), (400), (422), (511) and (440) crystalline planes, respectively.[24] For Fe–Ni–Co, the diffraction peaks are close to the standard card of $NiCo_2O_4$ (PDF#20-0781), but they all shift toward higher angles, suggesting a change in lattice spacing due to the formation of Fe–Ni–Co oxides.[25] Comparing the XRD pattern of the precursor (Fig. S1, ESI†), it can be seen that the intensity of the diffraction peak becomes larger, which indicates that the doping of iron changes the crystallinity of the NiCo microspheres. The diffraction peaks of Fe–Ni–Co are located between those of standard Fe, Co, and Ni, indicating the successful fabrication of highly crystalline Fe–Ni–Co.

As can be seen from Fig. 2 and Fig. S2 (ESI†), the precursor of the nickel-cobalt oxides is uniform nanospheres with a smooth surface. Comparison of Fig. 2a–h shows that, after iron doping, the morphological surface of the product becomes rough, and as the soaking time increases, more and more nanosheets grow on the nanosphere surface, forming beautiful flower-like nanospheres. When the soaking time reached 20 h, the nanosheets on the surface became thick compared with those at 15 h, and the surface pores were reduced. According to Fig. 2i and Fig. S5 (ESI†), the nanospheres grow a lot of small and filmy nanosheets on the surface, which is beneficial to increasing its specific surface area and facilitates the exposure of more active sites.[26,27] In addition, the pore formation is also conducive to the diffusion of the electrolyte and the release of gas products, thus improving its electrocatalytic performance.[28–30] The HRTEM image (Fig. 2j) shows that the spacing of lattice distance is 0.245 nm and 0.214 nm, corresponding to the (311) and (200) crystal facets of Fe–Ni–Co, respectively. The corresponding selected area electron diffraction (SAED) plots (Fig. 2k) show bright ring patterns matching (111), (220), (311), and (222), consistent with the XRD analysis.[31–33] The mapping plot of Fe–Ni–Co (Fig. 2l) illustrates the uniform distribution of Ni, Co, and Fe elements in the samples, consistent with the EDX analysis (Fig. S3, ESI†).

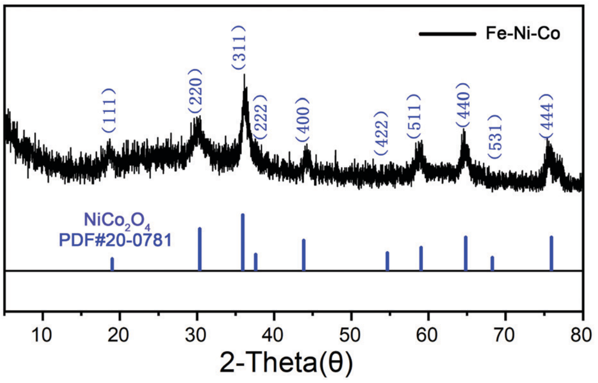

Fig. 1 XRD pattern of Fe–Ni–Co.

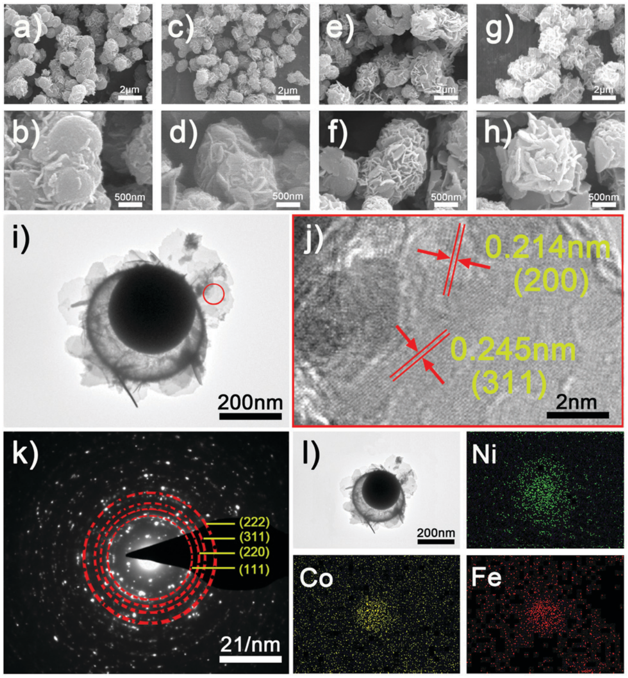

Fig. 2 SEM images of (a) and (b) FeNiCo-5, (c) and (d) FeNiCo-10, (e) and (f) FeNiCo-15, and (g) and (h) FeNiCo-20; (i) TEM images, (j) HRTEM images of the region marked with a red circle, (k) SAED pattern and (l) elemental mapping of FeNiCo-15.

The chemical composition and valence states of the elements in the samples were further explored using XPS. Fig. 3a shows that the sample is mainly composed of Ni, Co, Fe, and O elements, which is consistent with the characterization results described above. Comparing Fig. 3b and Fig. S4a (ESI†), before Fe doping, the Ni 2p had two strong peaks at 854.78 eV and 872.48 eV, ascribed to Ni^{2+} $2p_{3/2}$ and Ni^{2+} $2p_{1/2}$, respectively. After Fe doping, Ni 2p showed strong peaks at 855.28 eV, 854.98 eV and 872.68 eV, 873.58 eV, ascribed to Ni^{2+} $2p_{3/2}$, Ni^{3+} $2p_{3/2}$ and Ni^{2+} $2p_{1/2}$, Ni^{3+} $2p_{1/2}$, respectively. It was demonstrated that Ni^{3+} was generated by a redox reaction between the precursor and $FeSO_4$ *via* 15 h of soaking at room temperature.[34,35] Comparing Fig. 3c and Fig. S4b (ESI†), when iron has not been introduced, Co 2p had two strong peaks at 780.38 eV and 796.18 eV, ascribed to Co^{2+} $2p_{3/2}$ and Co^{2+} $2p_{1/2}$, whereas when iron was introduced, Co 2p showed diffraction peaks at 779.98 eV, 782.48 eV and 794.68 eV, 797.28 eV, ascribed to Co^{2+} $2p_{3/2}$, Co^{3+} $2p_{3/2}$ and Co^{2+} $2p_{1/2}$, Co^{3+} $2p_{1/2}$, respectively, which further demonstrates that there is a

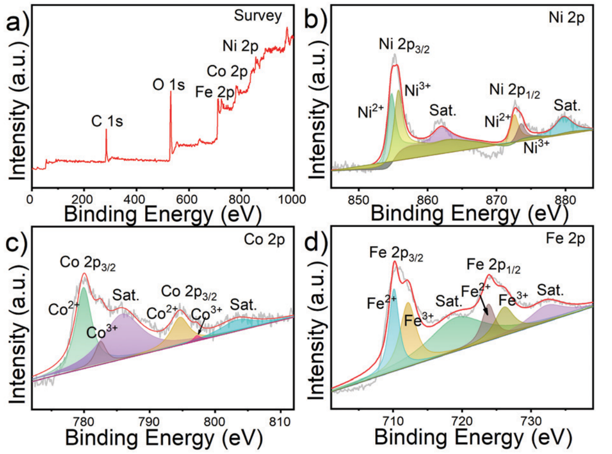

Fig. 3 (a) Survey, (b) Ni 2p, (c) Co 2p, and (d) Fe 2p XPS spectra of FeNiCo-15.

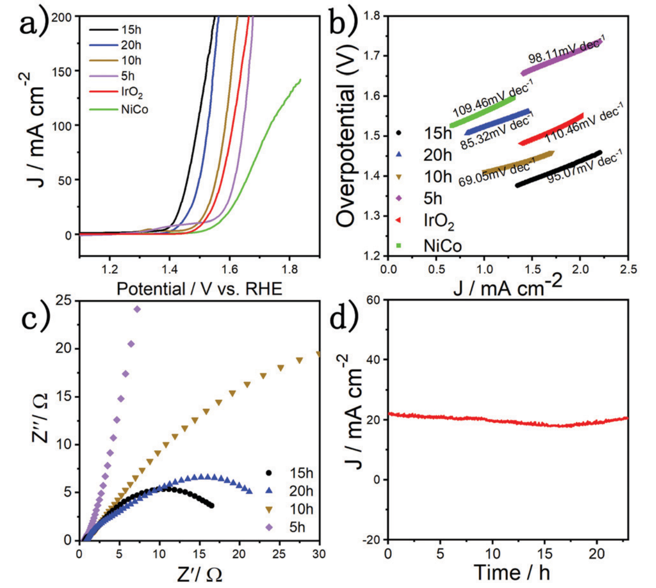

Fig. 4 (a) The polarization curves, (b) Tafel slopes, (c) Nyquist plots, and (d) long-term stability of different catalysts and IrO_2 toward the OER.

reciprocal redox relationship between Ni, Co, and Fe after soaking for 15 h at room temperature.[36–39] Peaks with binding energies of 710.18 eV, 712.08 eV and 723.88 eV, 726.18 eV belong to Fe 2p as shown in Fig. 3d, attributed to Fe^{2+} $2p_{3/2}$, Fe^{3+} $2p_{3/2}$ and Fe^{2+} $2p_{1/2}$, Fe^{3+} $2p_{1/2}$, respectively, and the ferrous ions of $FeSO_4$ were reduced to produce iron ions.[40,41] It can be seen that Fe was successfully introduced into the precursor mixture, and Fe–Ni–Co nanospheres with a yolk–shell structure were successfully prepared.

The electrocatalytic properties of the samples at different mixing times were tested in a 1.0 mol L^{-1} KOH solution in an alkaline medium with a standard three-electrode system. As a comparison, FeNiCo-20, FeNiCo-15, FeNiCo-10, FeNiCo-5, IrO_2 and the precursor (NiCo) were tested under the same experimental conditions. According to the linear sweep voltammetry (LSV) polarization curve of the OER (Fig. 4a), at the same current density (10 mA cm^{-2}), overpotential values of 216, 204, 263, 303 and 271 mV, respectively, were observed for FeNiCo-20, FeNiCo-15, FeNiCo-10, FeNiCo-5, and IrO_2, respectively. The overpotential of NiCo was 373 mV, much higher than those of the FeNiCo-15 samples. To drive a current density of 10 mA cm^{-2}, the FeNiCo-15 catalyst requires an overpotential (η) of only 204 mV, which is 22 and 69 mV lower than the overpotentials for FeNiCo-20 and FeNiCo-10, respectively. Furthermore, this catalyst outperforms the commercial IrO_2 catalyst in 1.0 M KOH. The overpotential at 10 mA cm^{-2} for FeNiCo-15 is 77 mV lower than that for the IrO_2 catalyst. These results support that the FeNiCo-15 catalyst is a very promising non-precious electrocatalyst for the OER.

The Tafel slope data obtained in terms of the Tafel equation ($\eta = \alpha + \beta\log[j]$, where η represents the overpotential, α is a constant, and β is the Tafel slope) were used to analyze the OER kinetics of these catalysts.[42] As shown in Fig. 4b, the Tafel slopes of FeNiCo-20, FeNiCo-15, FeNiCo-10, FeNiCo-5, IrO_2 and NiCo are 85.32 mV dec^{-1}, 69.05 mV dec^{-1}, 95.07 mV dec^{-1}, 98.11 mV dec^{-1}, 90.46 mV dec^{-1} and 109.46 mV dec^{-1}, respectively. Compared to single-metal-based catalysts, these Tafel slope data show that mixed metal complexes have dramatically improved OER kinetics. The Tafel slope is the slope of the linear part of the Tafel curve and calculated as: Tafel slope = $2.303RT/\alpha nF$, where R is the gas constant, T is the absolute temperature in K, α is the charge transfer coefficient, n is the number of electrons transferred, and F is the Faraday constant.[42] The Tafel slope of FeNiCo-15 is close to 60 mV dec^{-1}, revealing that the second electron transfer step is the rate-determining step for the OER.[43] Furthermore, electrochemical impedance measurements could be utilized to investigate the interfacial resistance of the four electrocatalysts (Fig. 4c). FeNiCo-15 showed a lower resistance than the other catalysts throughout the OER catalysis process, indicating that it has higher charge transfer capabilities. Furthermore, stability is an important factor in the catalyst's bulk water electrolysis. The long-term endurance of the catalyst was further investigated in bulk electrolysis of water at a specific overpotential. As show in Fig. 4d, the current density was maintained well after 23 hour tests, indicating that the FeNiCo-15 catalyst has robust stability towards water oxidation. FeNiCo-15 nanospheres can be employed as high-activity catalysts for the OER in alkaline media with a cost benefit due to their high catalytic activity and long-term stability.

To learn more about the catalytic activity of the FeNiCo-15 catalyst, we looked into its electrochemically active surface area (ECSA). The electrochemical double-layer capacitance has a common positive connection with the ECSA. The corresponding Cdl was calculated by performing cyclic voltammetry scans of the intervals shown in Fig. S6 (ESI†) where the redox reaction does not occur. The Cdl value of FeNiCo-5 was 4.39 mF cm^{-2}, but that of FeNiCo-15 (21.71 mF cm^{-2}) was comparatively high (Fig. S7, ESI†). Generally, a flat surface area of 1 cm^2 CC has an average specific capacitance value of

40 μF cm^{-2}. Therefore, the ECSA value can be converted by Cdl through the following equation:

$$\text{ECSA}= \text{Cdl } (\text{mF cm}^{-2})/0.04 \ (\text{mF cm}^{-2}) \qquad (2)$$

The ECSA values of FeNiCo-20, FeNiCo-15, FeNiCo-10, and FeNiCo-5 are 410, 542, 180, and 109, respectively. These results imply that FeNiCo-15 had a higher ECSA and more active catalytic sites, making it more suitable for the OER catalytic reaction.[44,45] The following equation was used to obtain the TOF (turnover frequency) of the OER electrocatalyst in order to investigate the effect of Fe doping on the intrinsic OER activity:

$$\text{TOF} = (J \times A)/(4 \times n \times F) \qquad (3)$$

where J is the OER current density, A is the surface area of the anode, and F is the Faraday constant. As shown in Fig. S8 (ESI†), under the same overpotential, the TOF of FeNiCo-15 was much higher than those of the other catalysts. For instance, when η = 350 mV, the TOF of FeNiCo-15 was 10.31 s^{-1}, which is 1.86 and 3.77 times those of FeNiCo-10 and FeNiCo-5, respectively. In general, Fe doping increased the OER activity of the nanospheres while changing the OER mechanism at the same time.[46]

A conventional three-electrode system was used to investigate the HER catalytic performance of the as-synthesised FeNiCo-15 catalyst in a 1.0 mol L^{-1} KOH aqueous solution. Several reference samples were also evaluated for comparison, including FeNiCo-20, FeNiCo-10, FeNiCo-5, and the commercial Pt/C (20%). The *iR*-corrected LSV curves of all samples are shown in Fig. 5a at 1600 r min^{-1} with 1 mV s^{-1}. With a low overpotential (η) of only 178 mV at a current density of 10 mA cm^{-2}, FeNiCo-15 has the strongest HER activity, which is lower than those of FeNiCo-5 (111 mV), FeNiCo-10 (84 mV), and FeNiCo-20 (27 mV). The Tafel slope was obtained to investigate the reaction kinetics during the HER (Fig. 5b). The Tafel slope of FeNiCo-15 is approximately 66 mV dec^{-1}, which is less than those of FeNiCo-5 (151 mV dec^{-1}), FeNiCo-10 (138 mV dec^{-1}), FeNiCo-20 (89 mV dec^{-1}) and Pt/C (89 mV dec^{-1}). This shows that the HER pathway is the Volmer–Tafel mechanism.[47] The FeNiCo-15 catalyst has a lower Tafel slope, indicating better HER kinetics. EIS was used to explore the kinetics between the electrode and the electrolyte in greater depth. The FeNiCo-15 catalyst had the lowest charge transfer resistance among all the samples (Fig. 5c), showing that the charge transfer is promoted. As a result, it has the potential to aid the progression of the HER.[48] Chronoamperometry was used to test the durability of the FeNiCo-15 catalyst. After a 20 h test, the catalyst retains 96.82 percent of its initial density (Fig. 5d).

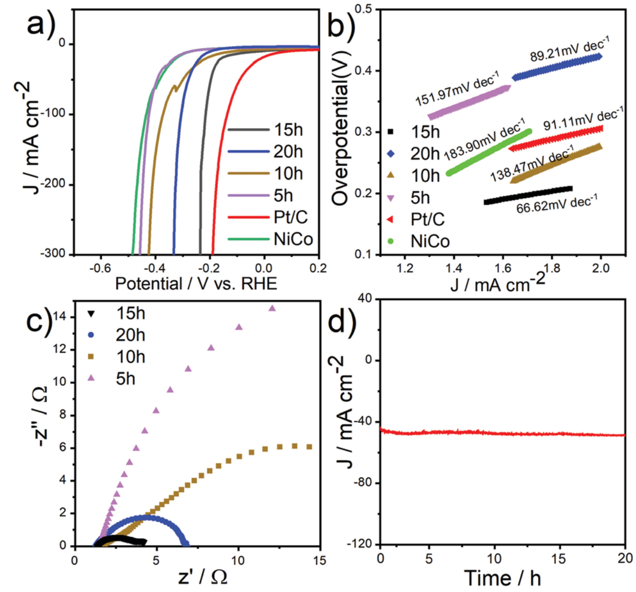

Fig. 5 (a) The polarization curves, (b) Tafel slopes, (c) Nyquist plots and (d) long-term stability of different catalysts and IrO_2 toward the HER.

The Cdl values of FeNiCo-15, FeNiCo-5, FeNiCo-10, and FeNiCo-10 were computed to further investigate the reasons for the increased HER activity of FeNiCo-15 in comparison to FeNiCo-5, FeNiCo-10, and FeNiCo-10. At varied scan rates, a CV between 0.236 and 0.336 V was used to derive the Cdl data (Fig. S9, ESI†). The Cdl values for FeNiCo-5, FeNiCo-10, FeNiCo-15, and FeNiCo-20 are 6.17, 8.85, 17.72, and 12.63 mF cm^{-2}, respectively, as shown in Fig. S10 (ESI†). We discovered that mixed metal complexes have substantially bigger HER electrochemically active surface areas than single-metal-based catalysts as a result of this finding.[49] The TOF values for the HER electrocatalysts can be calculated using the following equation to gain insight into the intrinsic HER activity:

$$\text{TOF} = (J \times A)/(2 \times n \times F) \qquad (4)$$

where J is the OER current density, A is the surface area of the anode, and F is the Faraday constant. As shown in Fig. S11 (ESI†), the TOF value of FeNiCo-15 at 0.2 V is 2.26 s^{-1}, which is 2 and 5 times higher than those of FeNiCo-20 and FeNiCo-10, respectively. According to Fig. S11b (ESI†), the TOFs for FeNiCo-10 and FeNiCo-20 are similar to that of FeNiCo-15, but the TOF for FeNiCo-5 is significantly lower. Based on the overpotential, Tafel slope, Rct, Cdl, and TOF, the FeNiCo-15 catalyst had a much better HER activity than single-metal-based catalysts (Table S3, ESI†).

According to the aforementioned electrochemical experiments, the FeNiCo-15 catalysts exhibit strong activity and robust stability towards both the HER and the OER. As a result, we created a two-electrode setup for full water splitting employing FeNiCo-15 catalysts loaded on carbon paper as the cathode and anode (FeNiCo-15|FeNiCo-15) and Pt|IrO_2 as the experimental control group. Full water splitting was done in 1.0 mol L^{-1} KOH at room temperature between 1 and 2 V with a scan rate of 2 mV s^{-1}. The cell voltage required to achieve a current density of 10 mA cm^{-2}, as shown in Fig. 6a, is 1.61 V, which is comparable to the integrated performance of the Pt|IrO_2 couple. The activity of the FeNiCo-15 catalyst is equivalent to that of several recently reported metal oxides and sulfides, demonstrating the superior activity of the FeNiCo-15 catalyst.[50,51] At a current density of 400 mA cm^{-2}, the FeNiCo-15|FeNiCo-15 and Pt|IrO_2 couples were tested for long-term

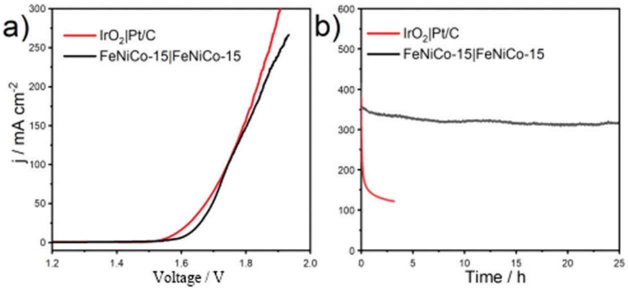

Fig. 6 (a) Polarization curves and (b) long-term stability of the FeNiCo-15|FeNiCo-15 and IrO_2|Pt/C couples.

stability, and the FeNiCo-15|FeNiCo-15 couple demonstrated more stable catalytic performance than Pt|IrO_2 at the same current density. After 25 h of observation, the current density of the FeNiCo-15|FeNiCo-15 couple did not change, as shown in Fig. 6b, indicating that the FeNiCo-15|FeNiCo-15 couple possesses robust stability toward full water splitting. However, the current density of Pt|IrO_2 rapidly decreases to about 30 mA cm^{-2} after 1 h. We characterized the samples after water electrolysis (Fig. S12 and S13, ESI†), the results show that the FeNiCo-15 bifunctional catalyst can be considered as a very promising material for applications in overall water splitting.

4 Conclusions

By using a self-template approach and ion exchange etching, unique Fe–Ni–Co ternary oxide hierarchical nanospheres with a yolk–shell structure were synthesized in this study. Due to its distinctive flake nanoflower shape and hierarchical yolk–shell structure, FeNiCo-15 has a greater specific surface area and exposes more active sites, which is helpful to electrocatalytic oxygen and hydrogen evolution reactions. When the current density is 10 mA cm^{-2} in 1.0 mol L^{-1} KOH electrolyte, the oxygen evolution overpotential and hydrogen evolution overpotential of FeNiCo-15 are 204 mV and 178 mV, while the Tafel slopes are 69.05 mV dec^{-1} and 66.62 mV dec^{-1}, respectively. FeNiCo-15 has demonstrated strong catalytic activity in electrocatalytic oxygen evolution reactions and hydrogen evolution reactions, and it can be employed as a dual-functional water electrolysis catalyst. The cell voltage required to achieve a current density of 10 mA cm^{-2} is 1.61 V, suggesting excellent activity and stability. In conclusion, the preparation of the FeNiCo-15 catalyst by the self-template method and ion exchange etching is a novel approach with high performance, and it is projected to become a useful bifunctional electrocatalyst in the field of water electrolysis.

Conflicts of interest

The authors declare no competing financial interest.

Acknowledgements

This work was supported by the Department of Education Basic Research Operating Costs of Heilongjiang Province, China (Grant No. 135309353).

Notes and references

1 N. K. Shrestha, S. A. Patil, J. Han, S. Cho, A. I. Inamdar, H. Kim and I. Hyunsik, *J. Mater. Chem. A*, 2022, **10**, 8989–9000.
2 B. You, M. T. Tang, C. Tsai, F. A. Pedersen, X. L. Zheng and H. Li, *Adv. Mater.*, 2019, **31**, 1807001.
3 X. C. Du, J. W. Huang, J. J. Zhang, Y. C. Yan, C. Y. Wu, Y. Hu, C. Y. Yan, T. Y. Lei, W. Chen, C. Fan and J. Xiong, *Angew. Chem., Int. Ed.*, 2019, **58**(14), 4484–4502.
4 Z. Y. Cai, X. M. Bu, P. Wang, J. C. Ho, J. Yangac and X. Y. Wang, *J. Mater. Chem. A*, 2019, **7**, 5069–5089.
5 Y. N. Guo, T. Park, J. W. Yi, J. Henzie, J. H. Kim, Z. L. Wang, B. Jiang, Y. Bando, Y. Sugahara, J. Tang and Y. Yamauchi, *Adv. Mater.*, 2019, **31**, 1807134.
6 P. Yu, F. M. Wang, T. A. Shif, X. Y. Zhan, X. D. Lou, F. Xia and J. He, *Nano Energy*, 2019, **58**, 244–276.
7 H. S. Park, J. Yang and M. K. Cho, *et al.*, *Nano Energy*, 2019, **55**, 49–58.
8 Y. T. Qu, B. X. Chen, Z. J. Li, X. Z. Duan, L. G. Wang, Y. Lin, T. W. Yuan, F. Y. Zhou, Y. D. Hu, Z. K. Yang, C. M. Zhao, J. Wang, C. Zhao, Y. M. Hu, G. Wu and Q. H. Zhang, *et al.*, *J. Am. Chem. Soc.*, 2019, **141**(11), 4505–4509.
9 X. X. Wang, C. Sun, F. He, E. Z. Liu, C. N. He, C. S. Shi, J. J. Li, J. W. Sha, S. H. Ji, L. Y. Ma and N. Q. Zhao, *ACS Appl. Mater. Interfaces*, 2019, **11**(35), 32460–32468.
10 Y. C. Jo, S. Cho, J. Seo, A. A. Ahmed, C. H. Lee, J. H. Seok, B. Hou, S. A. Patil, Y. Park, N. K. Shrestha, S. U. Lee, H. Kim and I. Hyunsik, *ACS Appl. Mater. Interfaces*, 2021, **13**, 53725–53735.
11 H. T. Bui, D. Y. Ahn, N. K. Shrestha, M. M. Sung, J. K. Leeb and S.-H. Han, *J. Mater. Chem. A*, 2016, **4**, 9781–9788.
12 H. J. Song, H. Yoon, B. Ju, G.-H. Lee and D.-W. Kim, *Adv. Energy Mater.*, 2018, **8**, 1802319.
13 J. G. Wang, W. Hua, M. Y. Li, H. Y. Liu, M. H. Shao and B. Q. Wei, *ACS Appl. Mater. Interfaces*, 2018, **10**(48), 41237–41245.
14 J. K. Das, A. K. Samantara, S. Satyarthy, C. S. Rout and J. N. Behera, *RSC Adv.*, 2020, **10**, 4650–4656.
15 S. J. Yoon, H. T. Bui, S. J. Lee, S. A. Patil, C. Bathula, N. K. Shrestha and I. Hyunsik, *J. Electroanal. Chem.*, 2020, **878**, 114594.
16 J. W. Zhu, Y. P. Huang, W. C. Mei, C. Y. Zhao, C. T. Zhang, J. Zhang, I. S. Amiinu and S. C. Mu, *Angew. Chem., Int. Ed.*, 2019, **58**(12), 3859–3864.
17 N. K. Shrestha, S. A. Patil, S. Cho, Y. C. Jo, H. S. Kim and I. Hyunsik, *J. Mater. Chem. A*, 2020, **8**, 24408–24418.
18 D. Vikraman, S. Hussain, L. Truong, K. Karuppasamy, H.-J. Kim, T. Maiyalagan, S.-H. Chun, J. W. Jung and H.-S. Kima, *Appl. Surf. Sci.*, 2019, **480**, 611–620.

19 S. J. Chu, W. Chen, G. L. Chen, J. Huang, R. Zhang, C. S. Song, X. Q. Wang, C. R. Li and K. Ostrikovc, *Appl. Catal., B*, 2019, **243**, 537–545.

20 G. Anandhababu, Y. Y. Huang, D. D. Babu, M. X. Wu and Y. B. Wang, *Adv. Funct. Mater.*, 2018, **28**(9), 1706120.

21 G. J. Hu, J. Li, P. Liu, X. Q. Zhu, X. F. Li, R. N. Ali and B. Xiang, *Appl. Surf. Sci.*, 2019, **463**, 275–282.

22 C. J. Yu, Y. N. Shi, F. Yan, Y. Y. Zhao, C. L. Zhu, X. L. Zhang, X. T. Zhang and Y. J. Chen, *Chem. Eng. J.*, 2021, **423**, 130240.

23 C. L. Zhu, Z. X. Yin, W. H. Lai, Y. Sun, L. N. Liu, X. T. Zhang, Y. J. Chen and S. L. Chou, *Adv. Energy Mater.*, 2018, **8**, 1802327.

24 D. F. Yan, S. Dou, L. Tao, Z. J. Liu, Z. G. Liu, J. Huo and S. Y. Wang, *J. Mater. Chem. A*, 2016, **4**, 13726–13730.

25 B. Geng, Y. Q. He, F. Yan, C. L. Zhu, X. L. Zhang, X. T. Zhang and Y. J. Chen, *Today Nano*, 2022, **18**, 100176.

26 L. H. Qu, Z. Y. Zhang, H. Zhang, H. Zhang and S. M. Dong, *Appl. Surf. Sci.*, 2018, **448**, 618–627.

27 Z. G. Meng, F. Xiao, Z. X. Wei, X. Y. Guo, Y. Zhu, Y. R. Liu, G. J. Li, Z. Q. Yu, M. H. Shao and W. Y. Wong, *Nano Res.*, 2019, **12**, 2954–2959.

28 A. Azhar, Y. Li, Z. X. Cai, M. Barakat Zakaria, M. K. Masud, S. A. Hossain, J. H. Kim, W. Zhang, J. B. Na, Y. Yamauchi and M. Hu, *Bull. Chem. Soc. Jpn.*, 2019, **92**, 875–904.

29 H. F. Wang, L. Y. Chen, H. Pang, S. Kaskel and Q. Xu, *Chem. Soc. Rev.*, 2020, **49**, 1414–1448.

30 C. N. R. Rao and K. Pramoda, *Bull. Chem. Soc. Jpn.*, 2019, **92**, 441–468.

31 Y. Lv, M. M. Han, W. B. Gong, D. D. Wang, C. Chen, G. Z. Wang, H. M. Zhang and H. J. Zhao, *Angew. Chem., Int. Ed.*, 2020, **59**, 23521–23526.

32 B. Geng, F. Yan, X. Zhang, Y. Q. He, C. L. Zhu, S. L. Chou, X. L. Zhang and Y. J. Chen, *Adv. Mater.*, 2021, **33**, 2106781.

33 C. Y. Su, H. Cheng, W. Li, Z. Q. Liu, N. Li, Z. F. Hou, F. Q. Bai, H. X. Zhang and T. Y. Ma, *Adv. Energy Mater.*, 2017, **7**, 1602420.

34 S. Sultan, J. N. Tiwari, J. H. Jang, A. M. Harzandi, F. Salehnia, S. J. Yoo and K. S. Kim, *Adv. Energy Mater.*, 2018, **8**, 1801002.

35 X. Zhang, F. Yan, X. Z. Ma, C. L. Zhu, Y. Wang, Y. Xie, S. L. Chou, Y. J. Huang and Y. J. Chen, *Adv. Energy Mater.*, 2021, **11**, 2102141.

36 W. Zhang, X. F. Jiang, X. B. Wang, Y. V. Kaneti, Y. X. Chen, J. Liu, J. S. Jiang, Y. Yamauchi and M. Hu, *Angew. Chem., Int. Ed.*, 2017, **56**, 8435–8440.

37 H. W. Gao, J. B. Zang, X. X. Liu, Y. H. Wang, P. F. Tian, S. Y. Zhou, S. W. Song, P. P. Chen and W. Li, *Appl. Surf. Sci.*, 2019, **494**, 101–110.

38 B. Yu, F. Qi, B. J. Zheng, J. H. Zhou and Y. F. Chen, *Electrochim. Acta*, 2018, **277**, 161–167.

39 L. N. Liu, Y. Wang, F. Yan, C. L. Zhu, B. Geng, Y. J. Chen and S. L. Chou, *Small Methods*, 2020, **4**, 1900571.

40 Y. Q. Yang, K. Zhang, H. L. Lin, X. Li, H. C. Chan, L. C. Yang and Q. S. Gao, *ACS Catal.*, 2017, **7**, 2357–2366.

41 Y. L. Huang, C. Q. Feng, H. M. Wu, S. F. Wang, F. Wang and H. K. Liu, *J. Mater. Sci.*, 2018, **53**, 1123–1134.

42 T. Chen, S. Z. Li, J. Wen, P. B. Gui, Y. X. Guo, C. Guan, J. P. Liu and G. J. Fang, *Small*, 2018, **14**, 1700979.

43 X. Wang, L. Yu, B. Y. Guan, S. Y. Song and X. W. Lou, *Adv. Mater.*, 2018, **30**, 1801211.

44 L. N. Liu, X. Zhang, F. Yan, B. Geng, C. L. Zhu and Y. J. Chen, *J. Mater. Chem. A*, 2020, **8**, 18162–18172.

45 Y. Wang, L. N. Liu, X. Zhang, F. Yan, C. L. Zhu and Y. J. Chen, *J. Mater. Chem. A*, 2019, **7**, 22412–22419.

46 Z. W. Fang, L. L. Peng, H. F. Lv, Y. Zhu, C. S. Yan, S. Q. Wang, P. Kalyani, X. J. Wu and G. H. Yu, *ACS Nano*, 2017, **11**(9), 9550–9557.

47 C. V. V. M. Gopi, A. E. Reddy and H. J. Kim, *J. Mater. Chem. A*, 2018, **6**, 7439–7448.

48 C. Gu, S. J. Hu, X. S. Zheng, M. R. Gao, Y. R. Zheng, L. Shi, Q. Gao, X. Zheng, W. S. Chu, H. B. Yao, J. F. Zhu and S. H. Yu, *Angew. Chem., Int. Ed.*, 2018, **57**, 4020–4024.

49 Z. X. Yin, S. Zhang, J. L. Li, S. K. Ma, W. Chen, X. Z. Ma, Y. Zhou, Z. F. Zhang and X. Wang, *New J. Chem.*, 2021, **45**, 12996–13003.

50 Z. X. Yin, S. Zhang, W. Chen, X. Z. Ma, Y. Zhou, Z. F. Zhang, X. Wang and J. L. Li, *New J. Chem.*, 2020, **44**, 17477–17482.

51 G. P. Liu, B. Wang, P. H. Ding, W. X. Wei, Y. Z. Ye, L. Wang, W. S. Zhu, H. M. Li and J. X. Xia, *J. Alloys Compd.*, 2020, **815**, 152470.